Journal of Alloys and Compounds 509S (2011) S87–S91

Contents lists available at ScienceDirect

Journal of Alloys and Compounds

journal homepage: www.elsevier.com/locate/jallcom

Indentation plastic work and large compression plasticity in *in situ* nanocrystallized $Zr_{62}Cu_{18}Ni_{10}Al_{10}$ bulk metallic glass

J. Fornell[a], S. Suriñach[a], M.D. Baró[a], J. Sort[b,a,*]

[a] Departament de Física, Universitat Autònoma de Barcelona, 08193 Bellaterra, Spain
[b] Institució Catalana de Recerca i Estudis Avançats and Departament de Física, Universitat Autònoma de Barcelona, 08193 Bellaterra, Spain

ARTICLE INFO

Article history:
Received 24 August 2010
Received in revised form 4 December 2010
Accepted 7 December 2010
Available online 14 December 2010

Keywords:
Metallic glasses
Microstructure
Mechanical properties
Nanoindentation
Transmission electron microscopy

ABSTRACT

Large plasticity is observed during uniaxial macroscopic compression of $Zr_{62}Cu_{18}Ni_{10}Al_{10}$ bulk metallic glass. Nanoindentation experiments, performed on the as-cast and compressed specimens, confirm the enhanced plasticity after compression. Indeed, the ratio between the plastic and the total indentation energies, U_{pl}/U_{tot}, is larger in the compressed sample than in the as-cast alloy. Furthermore, in both samples, U_{pl}/U_{tot} tends to progressively increase with the maximum indentation applied load, thus confirming the tendency towards enhanced plasticity as deformation proceeds. Transmission electron microscopy reveals that deformation (induced either by macroscopic compression tests or nanoindentation) causes partial nanocrystallization of the glass. This effect is likely to play a crucial role in the observed plasticity and also results in mechanical hardening.

1. Introduction

Due to their amorphous character and the concomitant lack of dislocations and grain boundaries, bulk metallic glasses (BMG) exhibit a variety of mechanical properties that are often superior to those of crystalline metals and ceramics. For example, they can be twice as strong as conventional steels, exhibit more elasticity than ceramics and be less brittle than most oxide glasses [1,2]. These materials also show good corrosion and wear resistance and can be easily deformed without fracture (i.e., similar to polymers) when heated within the supercooled liquid region (i.e., between the glass transition and the crystallization temperatures). However, unlike crystalline materials, the deformation behavior of metallic glasses at room temperature is usually inhomogeneous: plastic flow is accommodated in narrow shear bands originated from the coalescence of free volume. As a result, BMG usually fracture in a brittle manner with plastic strains lower than 2%.

In recent years, it has been reported that certain BMGs (e.g., some Zr-, Pd-, Pt- or Cu-based ones) can exhibit values of plastic deformation around 20% or more when compressed at room temperature [3–6]. Although there are some intrinsic parameters (e.g., high Poisson's ratio) that favor large plasticity and toughness [4,7], impressively large values of plastic strains have been mainly attributed to either nanoscale phase separation (i.e., chemical decomposition) [3,8] or nanocrystallization occurring by the combined action of the applied shear stresses and the temperature rise during deformation [6,9]. These local structural inhomogeneities favor multiple branching of shear bands, which interact with each other, thus avoiding catastrophic failure caused by rapid propagation of a single shear band. With the goal of enhancing plasticity, fine particles can be introduced *ex situ* (i.e., during casting) to form nanocomposite materials [10] or, as pursued in this work, nanocrystallization can be induced *in situ* during the course of deformation experiments. A significant plasticity enhancement can also be achieved by precise control of the residual stress by means of surface treatments, again with the aim of promoting extensive shear band activity [5].

The effects of plastic deformation (induced by bending, rolling, nanoindentation or macroscopic compression) on the microstructure and properties of bulk metallic glasses are, in fact, under discussion [1]. It is generally accepted that plastic flow leads to dilatation (i.e., creation of free volume) [11,12], an effect which has been characterized by different experimental techniques such as calorimetry, density measurements, synchrotron radiation or positron annihilation [13–15]. Dilatation causes mechanical softening leading, for example, to an indentation size effect [16,17]. Whether additional microstructural features occur upon deformation (phase separation, nanovoids formation or nanocrystallization) depends on the exact glass composition and the applied shear stress. In addition, several other factors, such as the temperature rise due to localized heating at shear bands, enhanced

* Corresponding author at: Departament de Física, Universitat Autònoma de Barcelona, 08193 Bellaterra, Spain. Tel.: +34 935811401; fax: +34 935812155.
E-mail address: jordi.sort@uab.es (J. Sort).

0925-8388/$ – see front matter © 2010 Elsevier B.V. All rights reserved.
doi:10.1016/j.jallcom.2010.12.045

atomic diffusion caused by excess free volume or presence of pre-existing quasicrystalline nuclei prior to deformation, can explain deformation-induced nanocrystallization. Contrary to the accumulation of free volume, nanocrystallization often causes mechanical hardening, an effect which has been recently investigated in several families of BMG [1,18,19].

In this work, we investigate the changes in microstructure and mechanical behavior (with particular emphasis on the induced plasticity) of $Zr_{62}Cu_{18}Ni_{10}Al_{10}$ bulk metallic glass during uniaxial macroscopic compression and nanoindentation. This alloy exhibits very large plasticity during compression tests. The normalized indentation plastic energy is larger in the compressed specimen than in the as-cast alloy and, remarkably, this energy increases with the indentation applied loads. These effects are ascribed to deformation-induced nanocrystallization, which is investigated in detail by transmission electron microscopy.

2. Materials and methods

A master alloy with composition $Zr_{62}Cu_{18}Ni_{10}Al_{10}$ was prepared by arc melting a mixture of the pure elements in an Ar atmosphere. Rods of 2 mm in diameter were obtained from the melt by copper mould casting. The amorphous character of the as-cast sample was verified by X-ray diffraction (XRD) and transmission electron microscopy (TEM) equipped with selected area electron diffraction (SAED). The thermal stability of the system was investigated by differential scanning calorimetry (DSC).

Macroscopic compression tests were performed on cylindrical specimens, cut to a perfect orthogonal geometry with an aspect ratio of 2:1, and measured at room temperature at an approximately constant loading rate of $1.8 \times 10^{-4}\ s^{-1}$. Care was particularly taken to ensure that both surfaces of the rod were initially flat and parallel to each other prior to the compression test. The compression experiment was carried out by placing the glassy rod between two WC platens which were also flat and parallel to each other. The overall plasticity of the alloy and the value of yield stress were evaluated from these macroscopic compression tests.

Nanoindentation experiments were performed at room temperature, in the load control mode, using a UMIS equipment from Fischer-Cripps Laboratories, equipped with a Berkovich pyramidal-shaped indenter tip, applying maximum loads ranging from 2 mN to 100 mN. A load holding period of 20 s was introduced in all cases before unloading and the thermal drift was always kept below $\pm 0.05\ nm\ s^{-1}$. A total of 30 indentations for each loading condition were performed to verify the accuracy of the indentation data. Prior to nanoindentation, the specimens were carefully polished to mirror-like appearance using diamond paste. The hardness values were evaluated at the beginning of the unloading segment, using the method of Oliver and Pharr [20], after proper corrections for the contact area, instrument compliance and initial penetration depth. The exact procedure used to measure H and E is based on the assumption that unloading is fully elastic. It can then be shown that the amount of material sink-in, h_s, during indentation is given by [20]:

$$h_s = \varsigma \frac{P_{max}}{S} \tag{1}$$

where ς is a constant that depends on the geometry of the indenter (and is equal to 0.75 for a Berkovich indenter) and S is the contact stiffness, which is calculated from the slope of the unloading curve:

$$S = \frac{dP}{dh} \tag{2}$$

It follows that the indentation contact depth can be expressed as:

$$h_c = h_{max} - \varsigma \frac{P_{max}}{S} \tag{3}$$

The projected contact area is then a function of the contact depth, i.e., $A = F(h_c)$. This function depends on the geometry of the indenter and for an ideal Berkovich indenter is given by:

$$A = 24.56\, h_c^2 \tag{4}$$

However, the area function must be carefully calibrated by independent measurements on a calibration sample (typically fused quartz) so that deviations from ideal sharp indenter geometry are taken into account. For the calibration, a series of indentations are made to different depths. The plot A versus h_c is then fitted using a polynomial function:

$$A = \sum_{n=0}^{8} C_n (h_c)^{2-n} \tag{5}$$

In this expression C_n are constants, where the first one, $C_0 = 24.56$ describes the perfect Berkovich indenter and the others describe deviations due to blunting of the tip.

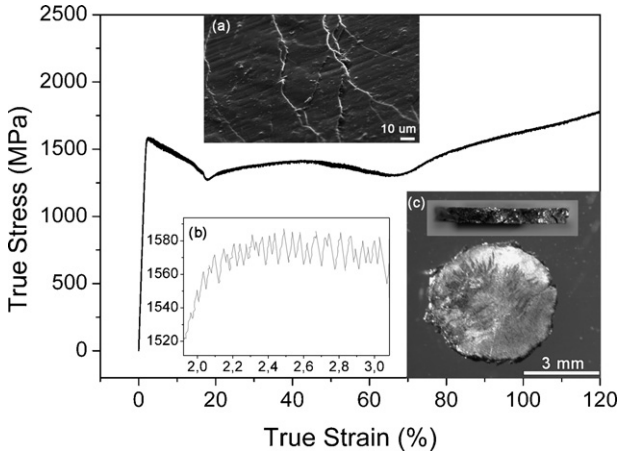

Fig. 1. The true strain–stress curve obtained from the uniaxial compression test of the as-cast $Zr_{62}Cu_{18}Ni_{10}Al_{10}$. Inset (a) is a scanning electron microscopy image showing the shear bands formed at the outer lateral surface of a compressed specimen. Inset (b) shows a magnified view of the serrated flow region of the compression test. Inset (c) shows optical microscopy images of the compressed specimen (cross sectional and lateral views).

Once the contact area and stiffness are calculated, the hardness and elastic modulus are readily obtained. The hardness is calculated using the following expression:

$$H = \frac{P_{max}}{A} \tag{6}$$

Evaluation of the elastic modulus follows from its relationship with the contact area and the measured unloading stiffness:

$$S = \beta \frac{2}{\sqrt{\pi}} E_r \sqrt{A} \tag{7}$$

where β is a constant that depends on the geometry of the indenter ($\beta = 1.034$ for a Berkovich indenter) and E_r is the so-called reduced elastic modulus defined by:

$$\frac{1}{E_r} = \frac{1-\nu^2}{E} + \frac{1-\nu_i^2}{E_i} \tag{8}$$

The reduced modulus takes into account the fact that elastic displacements occur in both the specimen, with Young's modulus E and Poisson's ratio ν, and the indenter, with elastic constants E_i and ν_i. Note that for diamond $E_i = 1141$ GPa and $\nu_i = 0.07$. Finally, the elastic and total energies during nanoindentation are calculated as the areas between the unloading curve and the displacement axis (U_{el}) and between the loading curve and the displacement axis (U_{tot}). The plastic energy, U_{pl}, is obviously the difference $U_{tot} - U_{el}$.

Transmission electron microscopy (TEM) observations, using a JEOL-2011 operating at an accelerating voltage of 200 kV, were carried out in the as-cast, compressed and indented specimens. In the latter case, thin disks of 2 mm in diameter were cut into 200 μm thick slices with a diamond bladed saw. These slices were mechanically polished to achieve a mirror-like appearance. After indentation, the center of the specimen was thinned down to 20 μm using a mechanical dimple from the side opposite to the indented surface. Ion milling was then performed, again only on the side opposite to the indented surface. Exactly the same cutting and polishing procedures were applied to prepare the as-cast and compressed/indented TEM specimens.

3. Results and discussion

The XRD pattern of the as-cast $Zr_{62}Cu_{18}Ni_{10}Al_{10}$ sample (not shown) consisted of broad diffraction halos without any detectable trace of crystalline peaks, indicating the amorphous nature of the sample. The DSC curve, measured on the as-cast sample at a heating rate of 40 K/min, revealed a glass transition at $T_g = 670$ K and a supercooled liquid region of 98 K.

Shown in Fig. 1 is the true stress–true strain curve obtained under uniaxial compression of the $Zr_{62}Cu_{18}Ni_{10}Al_{10}$ alloy. From the compression experiments, the values of yield stress, σ_y, and Young's modulus, E, are: $\sigma_y = 1.55$ GPa and $E = 86$ GPa. Remarkably, the sample was compressed without fracture up to 120% strain deformation. The compression curve shows some peculiarities (i.e., successive softening/hardening periods) which, as reported

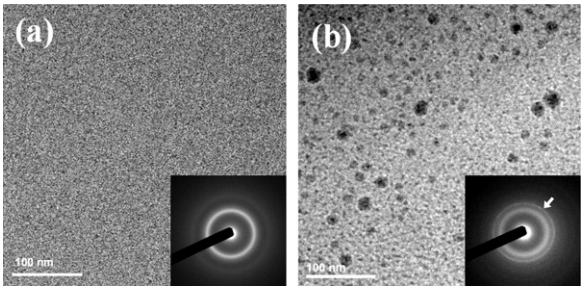

Fig. 2. Transmission electron microscopy (TEM) images of (a) the as-cast $Zr_{62}Cu_{18}Ni_{10}Al_{10}$ alloy and (b) the same alloy after being compressed up to 120%. The TEM images reveal the amorphous nature of the as-cast sample and the appearance of some nanocrystallites when the sample is compressed. The corresponding SAED patterns are shown in the insets.

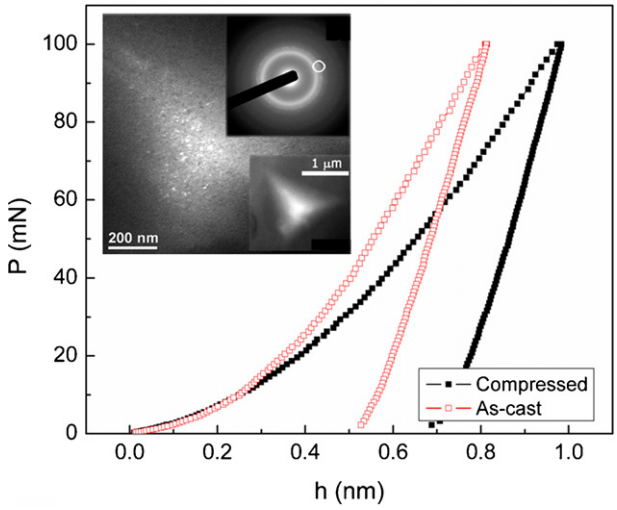

Fig. 3. Load–displacement (P–h) indentation curves (maximum load 100 mN) corresponding to the as-cast and compressed $Zr_{62}Cu_{18}Ni_{10}Al_{10}$ samples. Shown in the inset is a dark field TEM image of an indent performed using a maximum load of 10 mN. Together with the image is the selected area electron diffraction (SAED) pattern, with one of the rings marked in white, from which the dark field image was obtained. TEM images confirm the existence of nanocrystallites in the indented regions of the glass.

by other authors, have to be mainly ascribed to the increase of friction between the sample and the tungsten carbide platens due to the reduction of the length/width aspect ratio of the specimen [21,22]. This behavior is often encountered in BMG alloys exhibiting significant plasticity [3,22,23]. It should be noted that the final cross-sectional area of the compressed specimen is much larger than the initial one (i.e., increasing from 2 to approximately 4.5 mm, thus representing more than a two-fold increase) but the two surfaces of the disk-shaped specimen remain virtual parallel to each other after compression [see inset (c) in Fig. 1]. Inset (a) of Fig. 1 shows the occurrence of abundant shear bands at the outer surface of the compressed specimen. As a result, the stress–strain curve shows some serrations [see inset (b) in Fig. 1], as typically found in BMG during compression [1,17,24]. Note that shear bands form along various directions, sometimes bifurcating and intersecting each other. Furthermore, some shear bands exhibit wavy trajectories. This indicates that during their propagation, these bands encounter harder regions (presumably crystallites) and are forced to deviate. This avoids premature fracture of the specimen resulting from the rapid propagation of a single shear band, as it occurs in brittle BMG systems.

The great plasticity observed in this material should be ascribed to deformation-induced phase separation or nanocrystallization, since the Poisson's ratio of this alloy is not particularly large ($\nu = 0.378$), as compared to other BMG exhibiting much less plastic toughness. To shed light onto this issue, TEM imaging was performed on the as-cast and compressed specimens. Observation by TEM reveals a clear difference in the microstructures of both samples (Fig. 2). While the as-cast sample shows a homogeneous, featureless microstructure [Fig. 2(a)], the microstructure of the compressed samples [Fig. 2(b)] consists of a bright matrix containing darker embedded regions, with sizes around and below 10 nm. The fully amorphous structure of the as-cast specimen was confirmed by the selected area electron diffraction (SAED) pattern [see inset in Fig. 2(a)], where only amorphous halos were detected. Conversely, some diffraction rings could be observed in the SAED pattern of the compressed specimen [inset in Fig. 2(b)]. The second ring in the SAED pattern, indicated with an arrow in the inset of Fig. 2(b), is located at $d = 0.20$ nm, which agrees with the interplanar distance of the (3 1 0) planes in tetragonal Zr_2Ni (space group I4/mcm, $a = 0.649$ nm and $c = 0.527$ nm). The most intense ring of this phase, i.e. the (2 1 1) ring, would appear at $d = 0.254$ nm, thus coinciding with the amorphous halo [25]. It should be noted that Zr_2Ni is actually one of the first phases to crystallize during thermal annealing of Zr-based glasses with similar composition to the alloy investigated in our work [26]. Overall, the TEM results confirm that deformation promotes nanocrystallization of this Zr-based BMG.

In order to better understand the deformation behavior of the Zr-based metallic glass, nanoindentation tests were performed at different maximum applied loads (P_{max}) both in the as-cast and in the compressed specimen. Shown in Fig. 3 are the load–displacement indentation curves corresponding to $P_{max} = 100$ mN. It is remarkable that the maximum penetration depth is larger for the compressed disk than for the as-quenched rod. This may suggest the occurrence of a mechanical softening during deformation, an effect that is sometimes observed in BMG as a result of the net creation of free volume [16,17]. Actually, the overall dependence of hardness, H, on P_{max}, shown in Fig. 4(a), is somehow unexpected. Namely, although mechanical softening is indeed observed during indentation of the compressed specimen, H tends to progressively increase with P_{max} in the as-cast alloy. This effect has been recently investigated in detail and has been interpreted as a result of the competition between indentation-induced nanocrystallization, which induces mechanical hardening in the as-cast alloy, and the increase in the overall amount of free volume (and concomitant mechanical softening) with the applied indentation shear stress [18]. An example of nanocrystallization, induced by nanoindentation, is shown in the inset of Fig. 3 which is a dark-field TEM image from the diffraction spot highlighted in corresponding SAED pattern. The deformation-induced nanocrystals seem to be Zr_2Ni, the same phase as in the sample subjected to compression test. The Young's modulus obtained by nanoindentation is around 90 GPa for all indentation conditions, thus in good agreement with the value obtained from the macroscopic compression experiments.

It is also interesting to investigate the evolution of the elastic and plastic indentation energies as a function of P_{max}. It is rather obvious, already in Fig. 3, that the area between the load and the unload segments of the indentation curves (which is representative of U_{pl}) is larger in the compressed sample than in the as-cast alloy. The overall dependences of U_{el}, U_{pl} and U_{tot} on the maximum indentation load for both the as-cast and the compressed Zr-based alloys are shown in Fig. 5. As expected, all indentation energies increase with the applied load since the area underneath the load/unload segments also increases with P_{max}. However, it is remarkable that while a clear difference is observed in the evolution of U_{pl} when comparing the as-cast and compressed specimens, the dependence of U_{el} on P_{max} is virtually the same for both specimens. Consequently, the ratio U_{pl}/U_{tot} is larger in the compressed BMG

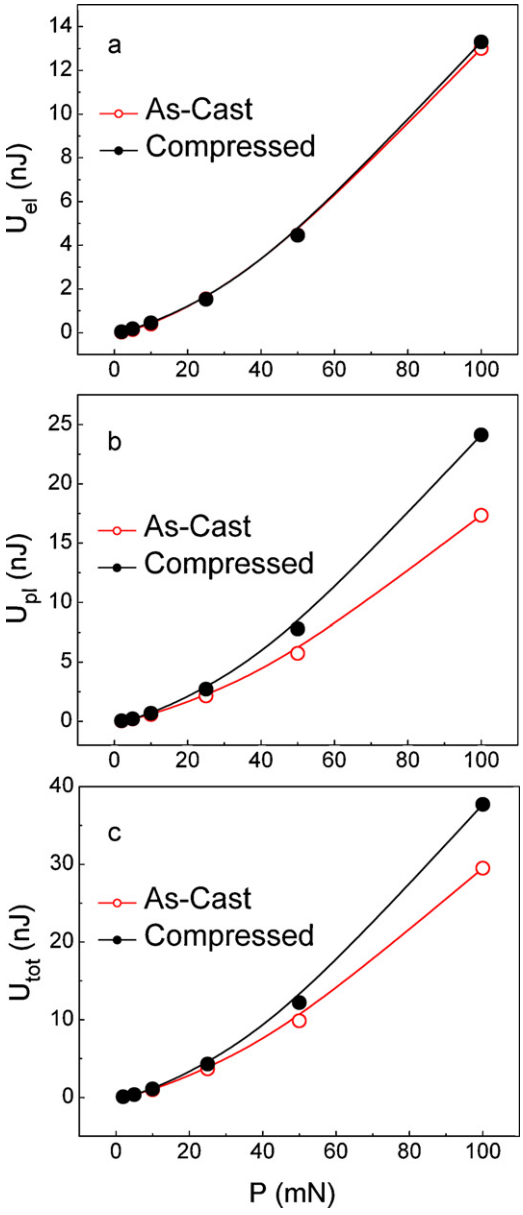

Fig. 4. Dependences of hardness, H, and the ratio U_{pl}/U_{tot} (where U_{pl} and U_{tot} denote, respectively, the plastic and total indentation energies), on the maximum applied load during indentation, P, for both the as-cast and the compressed $Zr_{62}Cu_{18}Ni_{10}Al_{10}$ samples. Note that error bars in H (±0.1 GPa) and U_{pl}/U_{tot} (±0.002) would be included within the size of the symbols.

than in the as-cast one [see Fig. 4(b)]. This result is in agreement with the enhancement of plasticity of the Zr-based BMG observed during macroscopic compression. Interestingly, the ratio U_{pl}/U_{tot} also increases with P_{max} (i.e., as indentation proceeds, particularly for loads smaller than 25 mN), both for the as-cast and for the compressed specimens [Fig. 4(b)]. It should be noted that the values of U_{pl}/U_{tot} shown in Fig. 4(b) are in agreement with those reported for $Zr_{50}Cu_{40}Al_{10}$ ($U_{pl}/U_{tot} \sim 0.6$ [27]) and $Cu_{46.25}Zr_{45.25}Al_{7.5}Er_1$ BMG ($U_{pl}/U_{tot} \sim 0.7$ [28]) and clearly larger than for brittle Fe-based BMG ($U_{pl}/U_{tot} \sim 0.37$ [19]). In fact, the ratio U_{pl}/U_{tot} has been sometimes used to characterize the mechanical behavior of brittle materials which are often difficult to test using macroscopic tensile tests [29]. Remarkably, most brittle materials (like ceramics) show relatively low U_{pl}/U_{tot} values (around 0.3–0.4 for SiC or Al_2O_3), whereas ductile metals (like Cu or Al) can show U_{pl}/U_{tot} values larger than 0.9 [29].

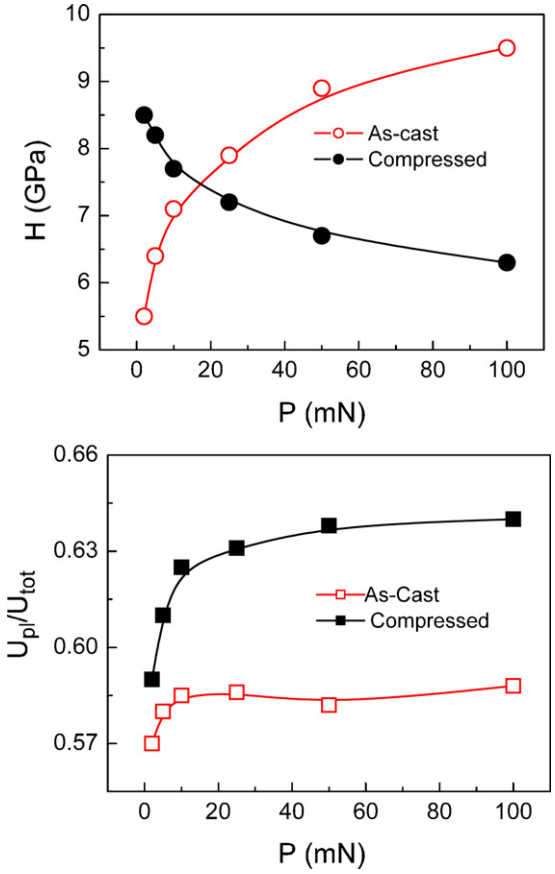

Fig. 5. Dependences of: (a) the elastic energy, U_{el}; (b) the plastic energy, U_{pl}; and (c) the total energy, U_{tot}, on the maximum applied load during indentation, P, for both the as-cast and the compressed $Zr_{62}Cu_{18}Ni_{10}Al_{10}$ samples. Note that the error bars would be included within the size of the symbols.

Similar to the interpretation for the large plasticity induced during uniaxial compression, the increase of the indentation plastic energy with the maximum applied load is likely to be related to deformation-induced nanocrystallization. In addition, the net creation of free volume induced by deformation [1,15–17], which enhances the overall atomic mobility and promotes the formation of shear bands (where excess free volume coalesces), can contribute as well to the observed increase of U_{pl}/U_{tot}. Finally, it should be noted that the ratio U_{el}/U_{tot} (where $U_{el} = U_{tot} - U_{pl}$) decreases after compression or as indentation proceeds, indicating that elastic recovery in BMG is susceptible to the prior deformation history of the glass. However, such a decrease in U_{el}/U_{tot} is mainly due to the increase of plastic energy induced by deformation, rather than to changes in U_{el}, as indicated in Fig. 5.

4. Conclusions

Nanoindentation measurements, performed on as-cast and compressed $Zr_{62}Cu_{18}Ni_{10}Al_{10}$ alloys, at different maximum applied loads, reveal an increase of plastic energy during deformation. For a given indentation load, the indentation plastic energy is also larger in the compressed specimen than in the as-cast alloy, while the elastic energy is similar for both cases. These trends in indentation plastic work are in agreement with the large plasticity observed during macroscopic compression tests of this material. Transmission electron microscopy showed the formation of nanocrystals after uniaxial compression and indentation, which presumably explains the observed large plastic strains.

Acknowledgements

Partial financial support from the Catalan DURSI (2009-SGR-1292 research project) and the Spanish Ministry of Science and Innovation (MAT 2007-61629 project) is acknowledged. We also thank the *Servei de Microscopia* of the *Universitat Autònoma de Barcelona* for the technical assistance during electron microscopy observations. M.D.B. acknowledges financial support from an ICREA-Academia award.

References

[1] C. Schuh, T. Hufnagel, U. Ramamurty, Acta Mater. 55 (2007) 4067–4109.
[2] M. Telford, Mater. Today 7 (2004) 36–43.
[3] Y.H. Liu, G. Wang, R.J. Wang, D.Q. Zhao, M.X. Pan, W.H. Wang, Science 315 (2007) 1385–1388.
[4] J. Schroers, W.L. Johnson, Phys. Rev. Lett. 93 (2004) 255506.
[5] Y. Zhang, W.H. Wang, A.L. Greer, Nat. Mater. 5 (2006) 857–860.
[6] J. Das, M.B. Tang, K.B. Kim, R. Theissmann, F. Baier, W.H. Wang, J. Eckert, Phys. Rev. Lett. 94 (2005) 205501.
[7] J.J. Lewandowsky, W.H. Wang, A.L. Greer, Philos. Mag. Lett. 85 (2005) 77–87.
[8] N. Van Steenberge, A. Concustell, J. Sort, J. Das, N. Mattern, A. Gebert, S. Suriñach, J. Eckert, M.D. Baró, Mater. Sci. Eng. A 491 (2008) 124–130.
[9] S.W. Lee, C.M. Lee, J.P. Ahn, Y.C. Kim, J.C. Lee, Mater. Sci. Eng. A 449 (2007) 172–175.
[10] H.C. Yim, R. Busch, U. Köster, W.L. Johnson, Acta Mater. 47 (1999) 2455–2462.
[11] F. Spaepen, Acta Metall. 25 (1977) 407–415.
[12] A.S. Argon, Acta Metall. 27 (1979) 47–58.
[13] A. Slipenyuk, J. Eckert, Scripta Mater. 50 (2004) 39–44.
[14] K.M. Flores, E. Sherer, A. Bharathula, H. Chen, Y.C. Jean, Acta Mater. 55 (2007) 3403–3411.
[15] B.P. Kanungo, S.C. Glade, P. Asoka-Kumar, K.M. Flores, Intermetallics 12 (2004) 1073–1080.
[16] N. Van Steenberge, J. Sort, A. Concustell, J. Das, S. Scudino, S. Suriñach, J. Eckert, M.D. Baró, Scripta Mater. 56 (2007) 605–608.
[17] J. Fornell, A. Concustell, S. Suriñach, W.H. Li, N. Cuadrado, A. Gebert, M.D. Baró, J. Sort, Int. J. Plast. 25 (2009) 1540–1559.
[18] J. Fornell, E. Rossinyol, S. Suriñach, M.D. Baró, W.H. Li, J. Sort, Scripta Mater. 62 (2010) 13–16.
[19] J. Fornell, S. González, E. Rossinyol, S. Suriñach, M.D. Baró, D.V. Louzguine-Luzgin, J.H. Perepezko, J. Sort, A. Inoue, Correlation between structural changes and enhanced mechanical properties during thermally-induced devitrification of Fe–Co–B–Si–Nb bulk metallic glass, Acta Mater. Acta Mater. 58 (2010) 6256–6266.
[20] W.C. Oliver, G.M. Pharr, J. Mater. Res. 7 (1992) 1564–1583.
[21] S.X. Song, H. Bei, J. Wadsworth, T.G. Nieh, Intermetallics 16 (2008) 813–818.
[22] H.M. Chen, X.H. Du, J.C. Huang, J.S.C. Jang, T.G. Nieh, Intermetallics 17 (2009) 330–335.
[23] F.H. Dalla Torre, A. Dubach, J. Schällibaum, J.F. Löffler, Acta Mater. 56 (2008) 4635–4646.
[24] C.A. Schuh, T.G. Nieh, Acta Mater. 51 (2003) 87–99.
[25] The Powder Diffraction File Database (PCPDFWIN v. 2.00), The International Centre for Diffraction Data, 1998.
[26] D. Zander, U. Köster, Mater. Sci. Eng. A 304–306 (2001) 292.
[27] A. Tekaya, S. Labdi, T. Benameur, A. Jellad, J. Mater. Sci. 44 (2009) 4930.
[28] F. Yang, D. Li, M.X. Yang, R. Li, W. Jiang, G. Wang, T. Zhang, P.K. Liaw, J. Phys. D: Appl. Phys. 42 (2009) 065401.
[29] Y.V. Milman, J. Phys. D: Appl. Phys. 41 (2008) 074013.